

Published in final edited form as:

*Nano Lett.* 2008 June ; 8(6): 1729–1735. doi:10.1021/nl0808132.

## Nanofluidic Biosensing for $\beta$ -amyloid Detection Using Surface Enhanced Raman Spectroscopy (SERS)

I-Hsien Chou, Melodie Benford, Hope T. Beier, and Gerard L. Côté\*

Department of Biomedical Engineering, Texas A&M University, College Station, TX 77843-3120, etonkimo@yahoo.com.tw, meb025@tamu.edu, hopebeier@tamu.edu, gcote@tamu.edu

Miao Wang, Nan Jing, and Jun Kameoka

Department of Electrical Engineering, Texas A&M University, College Station, TX 77843-3128, miao@tamu.edu, njing@neo.tamu.edu, kameoka@ece.tamu.edu

Theresa A. Good

Department of Chemical & Biochemical Engineering, University of Maryland Baltimore County, Baltimore, MD 21250, tgood@umbc.edu

### Abstract

Trace detection of the conformational transition of  $\beta$ -amyloid peptide ( $A\beta$ ) from a predominantly  $\alpha$ -helical structure to  $\beta$ -sheet could have a large impact in understanding and diagnosing Alzheimer's disease. We demonstrate how a novel nanofluidic biosensor using a controlled, reproducible surface enhanced Raman spectroscopy active site was developed to observe  $A\beta$  in different conformational states during the  $A\beta$  self-assembly process as well as to distinguish  $A\beta$  from confounder proteins commonly found in cerebral spinal fluid.

### Keywords

Surface Enhanced Raman Spectroscopy (SERS); Nanoparticles;  $\beta$ -Amyloid; Alzheimer's disease; Nanofluidic device; Nanochannel

Alzheimer's disease (AD), a progressive neurodegenerative disease and the leading cause of dementia in the aging population, affects 4.5 million people according to the 2000 US census<sup>1</sup>. One of the primary pathological hallmarks of Alzheimer's disease is the presence of insoluble neuritic plaques, composed primarily of  $\beta$ -amyloid peptide ( $A\beta$ ), in the cerebral cortex.  $A\beta$  peptide, a natural metabolic byproduct, results from the proteolytic cleavage of the amyloid precursor protein, either in the membrane or while undergoing endosomal processing. The resulting 39–42 amino acid long peptides are released into the extracellular space<sup>2–9</sup>. These species have a strong propensity to aggregate. Many hypothesize that aggregation of  $A\beta$  triggers a cascade of events that brings about neuritic dystrophy and neuronal death. Currently, Alzheimer's disease can only be diagnosed definitively by post-mortem identification of neuritic plaques and neurofibrillary tangles in central nervous system tissue. While methods exist for probable premortem diagnosis of AD, including *in vivo* imaging of the brain with magnetic resonance imaging or functional positron emission tomography, along with tests of cognitive and psychological function<sup>10, 11</sup>, reliable methods of premortem diagnosis are needed and may involve the use of biomarkers of AD such as  $A\beta$ .

\* Author to whom correspondence should be addressed: Phone: (979) 845-5494, Fax: (979) 845-4450.

The most prevalent species of A $\beta$  present in people with AD are A $\beta$  (1–40) and A $\beta$  (1–42). Both forms of A $\beta$  are found in cerebrospinal fluid (CSF) and blood plasma of all people, regardless of health.<sup>2–9</sup> A $\beta$  (1–40), the dominant peptide species, has a concentration of 5nM in CSF.<sup>3</sup> The relative concentrations of different A $\beta$  species including A $\beta$  (1–40), A $\beta$  (1–42), and their conformation/aggregation states change with the progression of disease.<sup>12</sup>

Most investigators believe that the cytotoxic species of A $\beta$  are one or more of the following species: soluble oligomers, A $\beta$  derived diffusible ligands (ADDL)<sup>7</sup>; protofibrils<sup>6, 13</sup>, and heterogeneous globular species.<sup>9</sup> These species arise during the misfolding and aggregation of the nontoxic, soluble A $\beta$  monomer that is predominantly  $\alpha$ -helical and random coil in structure to a conformational form of A $\beta$  with abundant  $\beta$ -pleated sheets (i.e. A $\beta$  fibrils and protofibrils).<sup>14–16</sup> However, the degree of neurotoxicity and relevance to disease progression of each conformational form of A $\beta$  is still under debate.<sup>17, 18</sup> Even the structure of the A $\beta$  fibril has only recently been elucidated (and not without some disagreement about the exact structure).<sup>19–22</sup> Needless to say, the structure of soluble A $\beta$  oligomers has not been determined.<sup>13, 23–25</sup> The development of tools useful in probing the structure of disease associated A $\beta$  species would be useful in the investigation of the molecular mechanisms of A $\beta$  cytotoxicity associated with AD.

The methods for probing the secondary and tertiary structure of proteins include Fourier transform infrared spectroscopy (FTIR), circular dichroism spectroscopy (CD), nuclear magnetic resonance (NMR) spectroscopy, and X-ray diffraction. X-ray diffraction and NMR have cumbersome preparation techniques. For FTIR, sampling is often difficult and has strong absorption due to water. X-ray diffraction and CD are limited by the state of the probed protein; molecules probed with X-ray diffraction must be crystallized, while the molecules must be in solution for CD. However, A $\beta$  does not crystallize, and toxic forms of A $\beta$  do not all stay in solution. Plus, CD lacks the sensitivity required to detect the lower range of toxic concentrations of A $\beta$ . Therefore, the development of a sensor platform that is able to detect structure specific oligomers of A $\beta$  along with conformational changes of the protein would be a valuable tool. Such a platform will help facilitate disease diagnosis and aid in understanding A $\beta$  assembly.

In the work presented here, the feasibility of using surface-enhanced Raman spectroscopy (SERS) to detect A $\beta$  (1–40), one of the two most prevalent A $\beta$  species in CSF, is addressed. Past protein studies involving Raman spectroscopy include probing particular amino acid residues in local environments, as well as structural investigation of proteins in biological samples.<sup>26–29</sup> However, Raman spectroscopy alone is not an efficient detection tool because of its low sensitivity, small optical cross-section, and the effects of intrinsic fluorescence and absorption of biomolecules on the spectra. Surface-enhanced Raman scattering can provide a significant enhancement of the Raman signal intensity of a molecule by several orders of magnitude ( $10^6$  to  $10^{12}$ ) through electromagnetic field enhancements and chemical enhancements due to adsorption of molecules onto metal surfaces. The effect of the electromagnetic enhancements are the best understood and believed to be the dominant mechanism responsible for the enhancements found in SERS.<sup>30, 31</sup> SERS enhancements of  $10^{12}$ – $10^{15}$  are observed when molecules of interest are adsorbed onto surfaces of gold nanoparticles, followed by electrolyte-induced aggregation.<sup>32</sup> However, such enhancements are observed only on certain unknown active spots or “hot spots” that provide the appropriate electromagnetic nano-environment, which has not been reproducible in the past, a major hindrance of aggregated particle-based substrates for biological applications. Recent advances in theory and computational techniques have shown that a strong electromagnetic field is invoked between solid nanoparticles, such as colloids, and at sharp boundaries of nanoscale geometries, such as on gratings and island films. Hence, many researchers have developed a well-ordered array of geometric nanoscale features on a substrate that can provide amplified

electromagnetic fields on these surfaces, thereby, expanding the use of SERS in analytical applications. For example, Van Duyne *et al.* reported strong enhancement factors for pyridine molecules adsorbed on metal film over nanosphere (MFON) electrodes, with silver deposited between the interstices formed by the removal of the nanoparticle arrays from the substrate.<sup>33</sup> However, random adsorption of molecules on the substrate is a critical drawback especially for the detection of biomolecules at trace levels.

To overcome the previously described limitations, we used a nanofluidic device that can significantly improve the reproducibility and sensitivity of SERS by exclusively localizing nanoparticles and increasing the concentration of target molecules at the entrance to the nanochannel. This nanofluidic device transports a mixture of target molecules and gold colloid (60 nm nanoparticles) down a microchannel to the entrance of a nanochannel. The 40 nanometer scale of the nanochannel depth causes size-dependent trapping of the gold colloid particles, creating a high density of gold nanoparticle clusters. In a similar fashion, the capillary flow induced by the device transports the target molecules through the interstices between the clusters, the SERS active sites, increasing the concentration of the target molecule and nanoparticles at the nanochannel entrance. The feasibility of using the nanofluidic biosensor has been previously reported for detecting nonresonant biomolecules at a concentration as low as 10 pM.<sup>34</sup> Thus, a SERS platform using a nanofluidic trapping device is described in this paper for the ultimate goal of facilitating diagnosis and understanding of Alzheimer's disease through the detection of Raman spectra that are conformation dependent and unique to A $\beta$  refolding from  $\alpha$ -helical to  $\beta$ -sheet structure.<sup>16</sup>

A $\beta$  (1–40) was synthesized and purified by BioSource International (Camarillo, CA). The sequence is DAEFRHDSGYEVHHQKLVFFADVGSNKGAIIGLMVGGVV. A $\beta$  was dissolved in DMSO to a concentration of 2.3 mM, aliquoted into micro-centrifuge tubes containing 5  $\mu$ L of solution, and stored in a –80 °C freezer until use. Then, 95  $\mu$ L of deionized water (DI water) was added to the A $\beta$  to create a 115  $\mu$ M stock solution. The A $\beta$  was stepwise diluted using DI water to the concentrations of interest before adding the gold colloid. A $\beta$  oligomer samples were prepared at concentrations ranging from 11.5 nM to 11.5 pM. The sample was observed at room temperature. Soluble A $\beta$  monomers (1.15nM) were prepared using the method described above and stored at 6 °C throughout observation period. Insulin (FW 5734) from bovine pancreas was purchased from Sigma-Aldrich Co. in powder form and was diluted to a concentration of 115  $\mu$ M in DI water then further diluted stepwise to a final concentration of 1.15 nM. Albumin (FW ~66,120) from bovine serum was purchased and purified by SIGMA ( $\geq$ 99% agarose gel electrophoresis). The albumin sample was prepared using the same procedure mentioned previously to a final concentration of 1.15 nM. The 2  $\mu$ m width nanochannel was used in the experiment comparing albumin, insulin, and A $\beta$ .

All protein SERS samples were prepared by mixing the protein with gold nanoparticles in solution (volume ratio 1:10). After mixing, 120  $\mu$ L of the gold colloid-protein mixture was then loaded immediately into the reservoir and observed over five days. Raman spectra were taken of the nanoparticle clusters every 12 hours over the course of observation. The residual samples were stored in the micro-centrifuge tubes for later pH measurement, determined by Thermo Orion pH Meter (Model 420, Thermo Scientific, Waltham, MA) with an AquaPro Combination pH Electrode. The accuracy was  $\pm$ 0.5 pH units. A pH of 6.8 was measured immediately after mixing and 6.4 after 48 hours for A $\beta$  samples, and insulin and albumin samples maintained a pH of 6.8 throughout the experiment.

All SERS spectra were collected using a Renishaw System 1000 Raman Spectrometer coupled to a Leica DMLM microscope (Schaunberg, IL). A 785 nm GaAlAs diode laser (SDL Model XC30) was used as the excitation laser and the SERS data were collected in 180° backscattered geometry. A 50X (NA = 0.75) air objective lens was used to deliver 8mW to the sample with

an approximate 2.2  $\mu\text{m}$  spot size. Raman scans were taken at the nanoparticle cluster and were integrated for 30 seconds over the range of 398 – 1608  $\text{cm}^{-1}$ . Each Raman spectrum was the average of seven consecutive scans from various locations at the entrance to the nanochannel. Although the Raman spectra were recorded in the 400–1600  $\text{cm}^{-1}$  range, no appreciable effect was observed below 500  $\text{cm}^{-1}$ . Accordingly, the spectra in the 500–1600  $\text{cm}^{-1}$  region are presented here. In addition, each figure showing multiple spectra has been artificially offset for visual clarity of the figure without any baseline correction or data smoothing.

### Aggregation of gold colloid using a nanofluidic device over time

The nanofluidic device is used to transport a mixture of target molecules and gold colloid (60 nm nanoparticles) down a microchannel to the entrance of a nanochannel. The nanometer scale of the nanochannel depth causes size-dependent trapping of the gold colloid particles (Fig. 1a), creating a high density of gold nanoparticle clusters. In a similar fashion, the capillary flow induced by the device transports the target molecules through the interstices between the clusters, the SERS active sites, increasing the concentration of the target molecule and nanoparticles at the nanochannel entrance. The configuration encourages size-dependent trapping of the gold nanoparticles and target molecules at the entrance to the shallow nanochannel, forming dense clusters with high local concentrations of target molecules (Fig. 1c). (The Nanofluidic device was fabricated by conventional top-down microfabrication techniques on a UV grade 500  $\mu\text{m}$ -thick fused silica wafer and the method of fabrication can be found in Supplementary Methods.)

To investigate the trapping properties of aggregated nanoparticles in the channel, gold colloid (60nm) was introduced into the nanofluidic device. Due to the capillary force of the channel, the nanoparticles in solution were transported down the deep microchannel. Since the diameter of the gold nanoparticle is larger (60 nm) than the depth of shallow nanochannel (40 nm), the nanoparticles were trapped at the nanochannel entrance and formed clusters within minutes. Figure 1 (d) shows the bright field image of an empty microchannel-nanochannel junction. Figure 1 (e) and (f) show nanoparticle clusters at the entrance to the nanochannel after loading the device with colloidal gold and taking images after 24 hours and 72 hours, respectively. Forming the clusters is reproducible and easily seen at the entrance to the nanochannel. The expansion of the aggregate size over time, as seen in a comparison of Figure 1 (e) to (f), indicates that the nanofluidic device maintains a capillary force over the 72 hours with only 120  $\mu\text{L}$  of solution. While the 24 to 72 hour lag time between loading the device and complete formation of the cluster needed for optimal SERS is substantial, we are exploring various electric pumping mechanisms as well as channel designs that should allow for full aggregation within minutes.

### Characterization of Nanofluidic System for SERS

The SERS approach used in this study is optimized by shifting the plasmon resonance frequency of the nanoparticle clusters to the near-infrared region to be in resonance with our excitation wavelength of 785nm. The use of near-infrared excitation is advantageous because water has low absorption in this range and this NIR range reduces native fluorescent background inherent to CSF. The shift in the localized plasmon resonance frequency at the site of the gold nanoparticle aggregate at the nanochannel entrance was probed, over three days, by light focused to a 33  $\mu\text{m}$  spot size (Fig. 1f). (The experimental setup for obtaining extinction spectrum of gold nanoparticle cluster is available in Supplementary Methods) Typical UV-Vis absorption and transmission spectra of gold colloid and gold nanoparticle clusters are shown in Figure 2. The extinction spectrum of gold colloid (Fig. 2b) exhibits a relatively sharp absorption band at 540 nm with a long tail trailing out toward longer wavelengths. Upon aggregation (Fig. 2a), the 540 nm band broadens and another large band appears around 800nm. The changes of the spectra, from minimal absorption and scattering properties to high

extinction at 800 nm, indicate that gold nanoparticles are clustered at the nanochannel entrance with up to 1500 times the optical density of the spectrum shown in Figure 2, according to Beer-Lambert's law. The microchannel has a depth of 6  $\mu\text{m}$ , whereas the path length of the cuvette used to measure the extinction spectrum of the gold colloid solution was 1 cm. Furthermore, we were unable to detect the extinction of gold colloid in the middle of microchannel, away from the aggregation at the nanochannel entrance (Curve C in Figure 2). This lack of signal is consistent with the observation that high-density gold nanoparticle clusters were formed only at the entrance to the nanochannel.

## Concentration Dependence of A $\beta$ SERS Spectra

We took SERS spectra, in the spectral range of 500–1600  $\text{cm}^{-1}$ , of A $\beta$  at three different concentrations (Fig. 3). The SERS Raman bands were assigned based on existing literature pertaining to the spectra of amino acids and proteins.<sup>34–38</sup> Table 1 illustrates the observed frequencies of several SERS bands. As expected, aromatic rings, amides, and carboxylic group vibrations dominate the SERS spectrum of A $\beta$ . In fact, shifts in the Amide III region, 1200 – 1300  $\text{cm}^{-1}$ , reflect the most compelling changes in proteins and are widely used to quantitatively explore secondary structure.<sup>25, 26, 28, 39</sup>

For a low concentration of A $\beta$  (11.5 pM), we observed Raman bands associated with the aromatic side chains at 1000, 1187, and 1488  $\text{cm}^{-1}$  (phenylalanine, tyrosine and phenylalanine, and histidine residues respectively), shown in Figure 3(a). A small shoulder band at 1036  $\text{cm}^{-1}$ , besides 1000  $\text{cm}^{-1}$ , supports the presence of phenylalanine in each sample. The presence of these bands indicates that the aromatic side chains are in a favorable position with respect to the gold nanoparticle surface. The phenylalanines, at amino acid 19 and 20 in the A $\beta$  sequence, are located in a region of the A $\beta$  peptide thought to be critical for A $\beta$  aggregation<sup>40</sup> and should only be available to interact with the metal surface in unaggregated forms of A $\beta$ . Furthermore, the histidine band at 1488  $\text{cm}^{-1}$  (Fig. 3a) is shifted about 10  $\text{cm}^{-1}$  from the assigned band in the literature,<sup>36</sup> which may have been altered due to protein-metal interactions, implying A $\beta$  interacts with the charged metal surface through its histidine molecules.<sup>41</sup> This histidine band and a band at 1266  $\text{cm}^{-1}$  (in the amide III region) suggests that A $\beta$  has an  $\alpha$ -helix structure.

At a higher concentration (1.15 nM), as seen in Figure 3(b), the band at 1266  $\text{cm}^{-1}$  diminishes while a new band appears at 1244  $\text{cm}^{-1}$  at a higher intensity. The red-shift from 1266  $\text{cm}^{-1}$  (assigned to the  $\alpha$ -helical structure) to 1244  $\text{cm}^{-1}$  (due to the  $\beta$ -sheet conformation), signifies that the proteins are in two different conformational states. With a concentration of 11.5 nM (Fig. 3c), the 1266  $\text{cm}^{-1}$  band is weak and hidden in the shoulder of the new broad band, a good indication that the polypeptide backbone of A $\beta$  has taken on a different conformation in close vicinity to the nanoparticle surface. Plus, the increase of the 961  $\text{cm}^{-1}$  mode (assigned to the C-C stretching mode in the hydrophobic segment of A $\beta$  polypeptide backbone) and the decrease in intensity of aromatic side chain signals are most likely due to the same refolding transition, which suggests that in the more aggregated  $\beta$ -sheet structure of A $\beta$ , the aromatic residues are no longer available to interact with the gold surface.<sup>41</sup> While most investigators would suggest that increasing the A $\beta$  concentration would result in conformational changes associated with aggregation, few have examined A $\beta$  aggregation at the concentrations used in these studies because of the limits of analytical tools used for structure determination.

Note that a presumable correlation between concentration and signal intensity of the SERS peaks is lacking due to the conformational dependence on concentration, making quantification of A $\beta$  oligomers difficult. Accordingly, we made no attempt to discern this correlation and focused on the associated structure changes in the protein with concentration. However,



quantification of A $\beta$  oligomers may be possible upon conduction of future, more careful experiments involving different concentrations of stable A $\beta$  oligomers added to the channel.

## Conformation Dependence of SERS Spectra

To confirm that the shifts in the spectral modes observed in Figure 3 at elevated concentrations were due to conformational changes rather than the sole effect of changes in concentration, we performed SERS on A $\beta$  as a soluble monomer and an oligomer or other aggregated species.

Figure 4(a) and (b) illustrate the SERS spectra of soluble A $\beta$  taken after residing in the nanofluidic device at 6°C for 38 and 48 hours, respectively. Others have shown that maintaining A $\beta$  at low temperatures prevents or significantly retards aggregation.<sup>44, 45</sup> An increase in intensity over time of the SERS bands (except the band 1000 cm<sup>-1</sup>) in Figure 4(a) and (b) can be attributed to an increase in concentration of the target molecules and in the density of the clusters due to the continuous flow of the device (as previously illustrated in Fig. 1). This sharpening feature may be due to a longer interaction time, allowing more A $\beta$  to bind to the surface of the nanoparticle. As also seen in Figure 3(a), a sharp band at 1266 cm<sup>-1</sup> is observed in Figure 4(a) and (b); due to the  $\alpha$ -helix structure adsorbing to the metal surface.<sup>36</sup> These spectra also exhibit distinct bands (seen previously in Figure 3) assigned to phenylalanine (1000 cm<sup>-1</sup>), histidine (1488 cm<sup>-1</sup>) and the tyrosine doublet (823 and 856 cm<sup>-1</sup>).

In Figure 4(c) and (d), the spectra of A $\beta$  oligomer, prepared by allowing A $\beta$  to aggregate at room temperature, contain similar qualities which are in contrast to the soluble monomers of Figure 4(a) and (b), such as a relatively strong band at 1244 cm<sup>-1</sup> (Fig. 4d) and 1266 cm<sup>-1</sup> (Fig. 4c). As explained in the previous section, the shift in the amide bands, from a mode characteristic of  $\alpha$ -helix to  $\beta$ -sheet, signifies conformational changes in the A $\beta$  peptide typical of the transition from soluble monomer to protofibrils or fibrils upon incubation.<sup>8, 15, 17, 46</sup> A strong band at around 1244 cm<sup>-1</sup> associated with  $\beta$ -sheet structure has been observed.<sup>35, 42, 43</sup> Furthermore, the presence of the amide III modes (1244 and 1266 cm<sup>-1</sup>) in Figure 4(c) confirms that the A $\beta$  was in the midst of A $\beta$  fibrillogenesis. If we further compare Figure 4(d) and Figure 3(c), spectral similarities attributed to  $\beta$ -sheets (675 and 1244 cm<sup>-1</sup> modes) and phenylalanine suggest that A $\beta$  at 11.5 nM had appreciable  $\beta$ -pleated sheets after 24 hours. It is difficult to predict *a priori* the effect that the metal surface may have on protein structure or how the metal surface will alter the kinetics of a self-association process, such as the A $\beta$  aggregation under investigation in this study. Thus, while we cannot directly compare our experimental conditions to other A $\beta$  aggregation experiments in solution, the general conclusions of others regarding the factors affecting aggregation should still apply. Namely, aggregation should be the predominant intermolecular interaction at high concentrations and reduced temperature should retard all intra- and intermolecular interactions.

## A $\beta$ and Confounder Proteins in CSF

To test the feasibility of detecting A $\beta$  in the presence of confounder proteins, SERS spectra of insulin and albumin were taken using the nanofluidic device and are shown in Figure 5. Figure 5(a) is the A $\beta$  oligomer or aggregated species. The 675 cm<sup>-1</sup> band has a stronger intensity in the spectra of the insoluble A $\beta$  oligomer than in the spectra of insulin (Fig. 5b) and albumin (Fig. 5c). Albumin (Fig. 5c) is known to have a structure consisting of around 55%  $\alpha$ -helices and 45% random coil.<sup>47</sup> The amide III band at 1294 cm<sup>-1</sup>, rather than at 1244 cm<sup>-1</sup>, could be due to modified Raman selection rules due to the  $\alpha$ -helix not directly adsorbed to the metal surface because of the folding complexity of the protein. Albumin also shows strong bands associated with tyrosine, phenylalanine and tryptophan (832, 856, 1000, 1030, 1185, and 1580 cm<sup>-1</sup>), indicating that albumin is adsorbed onto the nanoparticle surfaces via its aromatic side chains. Insulin (Fig. 5c) consists of two polypeptide chains joined with two cysteine disulfide bonds, with one disulfide bond involved in an intra-chain link. Although the C-S vibrations

(654  $\text{cm}^{-1}$ ) are overlapped by the broad band at 675  $\text{cm}^{-1}$ , the spectrum of insulin is still distinguishable from spectra of other proteins due to the S-S stretching mode at 549  $\text{cm}^{-1}$ . Despite these spectral differences, we may also need to employ advanced signal processing and multivariate statistical techniques to ultimately distinguish A $\beta$  in a complex media, or alternatively, functionalize the gold particles with specific markers for A $\beta$ .

A method of quantitatively assessing changes in a protein's structural conformation involves using a ratiometric measurement of the spectral height of amide III bands relative to some band (such as the CH<sub>2</sub> bending mode at 1455  $\text{cm}^{-1}$ ) whose intensity is independent of conformational content.<sup>26</sup> Taking ratiometric measurements of these bands gives ratios of 1.070, 1.223, 1.207, and 1.154 for A $\beta$  monomer, A $\beta$  oligomer, insulin, and albumin, respectively. The larger fraction indicates that more  $\beta$ -sheet and random coil structural elements are present in the protein. Consequently, we may be able to distinguish confounder proteins from A $\beta$  by their ratiometric spectral intensities and the absence and presence of certain Raman modes pertaining to amino acid residues in the protein available to interact with the metal surface.

A key feature of this nanofluidic device, is its ability to effectively trap nanoparticles at a specific region and confine the target molecules in the gap region of the particle clusters. Even though nanoparticle aggregation is not necessarily required for observing SERS signals of target molecules, aggregation is employed to observe stronger Raman enhancements from target molecules with a low optical scattering cross section, such as the proteins investigated here. In previous work from this laboratory, A $\beta$  could not be consistently detected using SERS without the aid of a secondary detection molecule of higher optical scattering cross section than most proteins.<sup>48</sup> In addition, our approach takes advantage of the enhancements while also providing consistent and reproducible nanoparticle aggregates in a specific location. The nanoparticle aggregates provide an environment for the target molecules to be concentrated in proximity to active sites (e.g., between adjacent nanoparticles or local resonant nanostructures) and exposed to the induced electromagnetic field simultaneously. The resulting platform overcomes the problem of random localized "hot spots" persistent in previous approaches to SERS platforms.

We have demonstrated a nanofluidic trapping device with the ability to encourage aggregation of gold nanoparticles without the need of electrolytes. Compared to other SERS techniques, our nanofluidic device is favorable for A $\beta$  detection for several reasons: (1) The SERS active environment is highly reproducible since nanoparticle-molecule clusters are always aggregated at the same, specific location, namely the entrance to the nanochannel. (2) Our device has a higher sensitivity than other SERS substrates because the target molecules become more concentrated over time at the entrance to the nanochannel. (3) The bioactivity of A $\beta$  is preserved, allowing the protein to undergo conformational changes. Therefore, we can probe proteins in solution without modifying the protein, implying direct detection of A $\beta$  in cerebrospinal fluid. Furthermore, our system's sensitivity to distinguishing between  $\alpha$ -helices and  $\beta$ -sheets as well as other protein conformational changes facilitates the discrimination between harmless monomeric forms of A $\beta$  and more toxic  $\beta$ -sheet oligomeric or protofibril/fibril forms. Tools such as the one described here may be valuable in the detection and structure determination of A $\beta$  associated with the progression of Alzheimer's disease.

## Supplementary Material

Refer to Web version on PubMed Central for supplementary material.

## Acknowledgements

The authors acknowledge the support of the National Institutes of Health (grant no. R21-NS050346-01). Hope Beier and Melodie Benford acknowledge the support of the National Science Foundation Graduate Research Fellowship.

## References

1. Hebert LE, Scherr PA, Bienas JL, Bennett DA, Evans DA. Archives of Neurology 2003;60:1119–1122. [PubMed: 12925369]
2. Hardy J, Selkoe DJ. Science 2002;297:353–356. [PubMed: 12130773]
3. Selkoe DJ. Physiological Reviews 2001;81:741–766. [PubMed: 11274343]
4. Mattson MP, Mark RJ, Furukawa K, Bruce AJ. Chemical Research in Toxicology 1997;10:507–517. [PubMed: 9168247]
5. Varadarajan S, Yatin S, Aksenova M, Butterfield DA. Journal of Structural Biology 2000;130:184–208. [PubMed: 10940225]
6. Wang SSS, Rymer DL, Good TA. The Journal of Biological Chemistry 2001;276:42027–42034. [PubMed: 11557751]
7. Gong Y, Chang L, Viola KL, Lacor PN, Lambert MP, Finch CE, Krafft GA, Klein WL. Proceedings of the National Academy of Sciences of the United States of America 2003;100:10417–10422. [PubMed: 12925731]
8. Ariga T, Kobayashi K, Hasegawa A, Kiso M, Ishida H, Miyatake T. Archives of Biochemistry and Biophysics 2001;388:225–230. [PubMed: 11368158]
9. Lee S, Fernandez EJ, Good TA. Protein Science 2007;16:723–732. [PubMed: 17327396]
10. Davis PC, Gray L, Albert M, Wilkinson W, Hughes J, Heyman A, Gado M, Kumar AJ, Destian S, Lee C, Duvall E, Kido D, Nelson MJ, Bello J, Weathers S, Jolesz F, Kikinis R, Brooks M. Neurology 1992;42:1676–1680. [PubMed: 1513454]
11. Duara R, Grady C, Haxby J, Sundaram M, Cutler NR, Heston L, Moore A, Schlageter N, Larson S, Rapoport SI. Neurology 1986;36:879–887. [PubMed: 3487046]
12. Bibl M, Mollenhauer B, Esselmann H, Lewczuk P, Klafki HW, Sparbier K, Smirnov A, Cepek L, Trenkwalder C, R  ther E, Kornhuber J, Otto M, Wiltfang J. Brain 2006;129:1177–1187. [PubMed: 16600985]
13. Wang SSS, Tobler SA, Good TA, Fernandez EJ. Biochemistry 2003;42:9507–9514. [PubMed: 12899638]
14. Takano K, Endo S, Mukaiyama A, Chon H, Matsumura H, Koga Y, Kanaya S. Febs Journal 2006;273:150–158. [PubMed: 16367755]
15. Lansbury PT. Neuron 1997;19:1151–1154. [PubMed: 9427238]
16. Kirkitadze MD, Condrion MM, Teplow DB. J Mol Biol 2001;312:1103–1119. [PubMed: 11580253]
17. Kaye R, Head E, Thompson JL, McIntire TM, Milton SC, Cotman CW, Glabe CG. Science 2003;300:486–489. [PubMed: 12702875]
18. Dahlgren KN, Manelli AM, Stine WB Jr, Baker LK, Krafft GA, LaDu MJ. Journal of Biological Chemistry 2002;277:32046–32053.
19. Petkova AT, Yau WM, Tycko R. Biochemistry 2006;45:498–512. [PubMed: 16401079]
20. Shivaprasad S, Wetzel R. J Biol Chem 2006;281:993–1000. [PubMed: 16263715]
21. Williams AD, Shivaprasad S, Wetzel R. Journal of Molecular Biology 2006;357:1283–1294. [PubMed: 16476445]
22. Williams AD, Portelius E, Kheterpal I, Guo J-t, Cook KD, Xu Y, Wetzel R. J Mol Biol 2004;335:833–842. [PubMed: 14687578]
23. Huang THJ, Yang DS, Plaskos NP, Go S, Yip CM, Fraser PE, Chakrabartty A. Journal of Molecular Biology 2000;297:73–87. [PubMed: 10704308]
24. Ward RV, Jennings KH, Jepras R, Neville W, Owen DE, Hawkins J, Christie G, Davis JB, George A, Karran EH, Howlett DR. Biochem 2000;348:137–144.
25. Takano K, Endo S, Mukaiyama A, Chon H, Matsumura H, Koga Y, Kanaya S. Febs J 2006;273:150–158. [PubMed: 16367755]
26. Frushour BG, Koenig JL. Biopolymers 1974;13:1809–1819. [PubMed: 4415467]
27. Lippert JL, Tyminski D, Desmeules PJ. Journal of the American Chemical Society 1976;98:7075–7080. [PubMed: 965667]
28. Kitagawa T, Azuma T, Hamaguchi K. Biopolymers 1979;18:451–465.



29. Yu NT, Liu CS, O'Shea DC. *Journal of Molecular Biology* 1972;70:117–132. [PubMed: 4672486]
30. Kneipp K, Kneipp H, Itzkan I, Dasari RR, Feld MS. *Journal of Physics:Condensed Matter* 2002;14:597–624.
31. Campion A, Kambhampati P. *Chemical Society Reviews* 1998;27:241–250.
32. Kneipp K, Kneipp H, Manoharan R, Hanlon EB, Itzkan I, Dasari RR, Feld MS. *Applied Spectroscopy* 1998;52:1493–1497.
33. Dick LA, McFarland AD, Haynes CL, Van Duyne RP. *Journal of Physical Chemistry B* 2002;106:854–860.
34. Wang M, Jing N, Chou IH, Cote' GL, Kameoka J. *Lab on a Chip* 2007;7:630–632. [PubMed: 17476383]
35. Beier HT, Cowan CB, Chou IH, Pallikal J, Henry JE, Benford ME, Jackson JB, Good TA, Coté GL. *Plasmonics* 2007;55–64.
36. Ortiz C, Zhang D, Xie Y, Davisson VJ, Ben-Amotz D. *Analytical Biochemistry* 2004;332:245–252. [PubMed: 15325292]
37. Podstawka EP, Ozaki Y, Proniewicz LM. *Applied Spectroscopy* 2004;58:570–580. [PubMed: 15165334]
38. Kumar GVP, Reddy BAA, Arif M, Kundu TK, Narayana C. *Journal of Physical Chemistry B* 2006;110:16787–16792.
39. Drachev VP, Thoreson MD, Khaliullin EN, Davisson VJ, Shalaev VM. *Journal of Physical Chemistry B* 2004;108:18046–18052.
40. Cavalu S, Cintă-Pinzaru S, Leopold N, Kiefer W. *Biopolymers* 2001;62:341–348. [PubMed: 11857273]
41. Asher SA, Ianoul A, Mix G, Boyden MN, Karnoup A, Diem M, Schweitzer-Stenner R. *J Am Chem Soc* 2001;123:11775–11781. [PubMed: 11716734]
42. Wetzell R, Shivaprasad S, Williams AD. *Biochemistry* 2007;46:1–10. [PubMed: 17198370]
43. Giacomelli CE, Norde W. *Macromolecular Bioscience* 2005;5:401–407. [PubMed: 15889393]
44. Meinke JH, Hansmann UHE. *J Chem Phys* 2007;126:0147061–0147065.
45. Sasahara K, Yagi H, Naiki H, Goto Y. *Biochemistry* 2007;46:3286–3293. [PubMed: 17316024]
46. Zirah S, Kozin SA, Mazur AK, Blond A, Cheminant M, Ségalas-Milazzo I, Debey P, Rebuffat S. *Journal of Biological Chemistry* 2006;281:2151–2161. [PubMed: 16301322]
47. Miura T, Suzuki K, Kohata N, Takeuchi H. *Biochemistry* 2000;39:7024–7031. [PubMed: 10841784]
48. Miura T, Thomas GJ Jr. *Subcell Biochem* 1995;24:55–99. [PubMed: 7900183]
49. Yu NT. *J Am Chem Soc* 1974;96:4664–4668. [PubMed: 4851109]

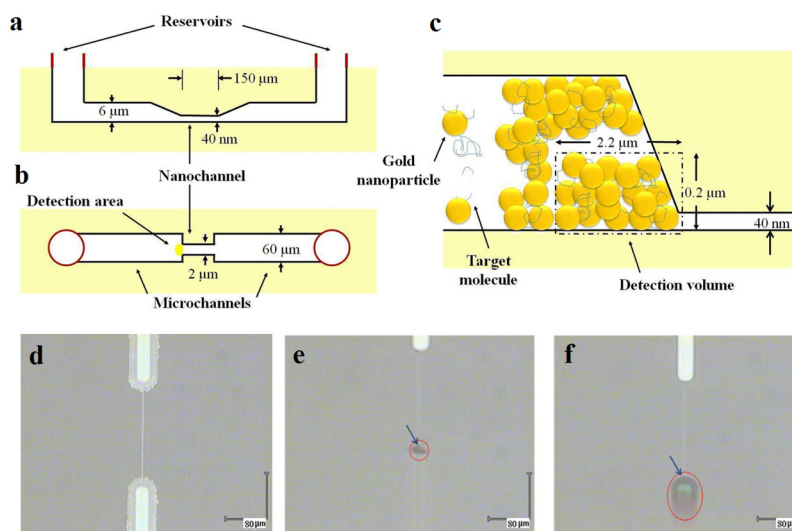


**Figure 1.**

Schematic diagram of a nanofluidic biosensor: (a) lateral view, (b) top view, and (c) expanded lateral view of a nanofluidic biosensor with aggregated nanoparticle SERS active clusters formed at the step structure. The nanochannel depth (40 nm) precludes entry of the nanoparticles (60 nm in diameter) into the nanochannel, thus inducing aggregation of the nanoparticles and target molecules. Brightfield microscope images of (d) an empty nanofluidic device consisting of a nanochannel between two microchannels, (e) nanoparticle clusters at the entrance to the nanochannel 24 hours and (f) 72 hours after being loaded with 120  $\mu\text{L}$  of gold colloid solution. The red circles in the images show an increase in aggregation size of the nanoparticles over time. The arrows indicate the entrance to the nanochannel. The gold colloid was introduced into the nanofluidic device from the plastic reservoir covering the inlet holes, which is shown in (a).

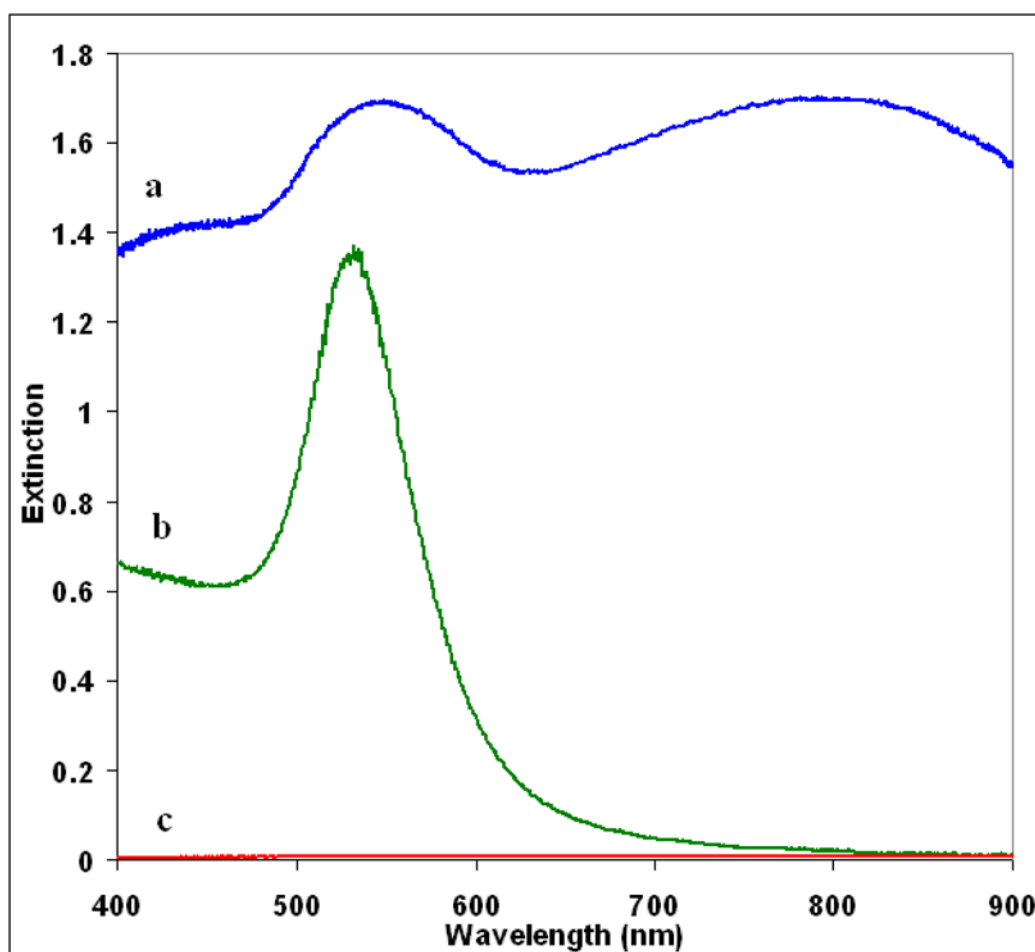


**Figure 2.**

(a) Extinction spectra of gold nanoparticle clusters at the entrance of the nanochannel, (b) extinction spectra of gold colloid in a cuvette, and (c) extinction spectra collected in the middle of the microchannel channel. Note the broadening and shift in the 540 nm gold colloid peak upon aggregation at the nanochannel entrance. No extinction was detected in the microchannel away from the nanochannel entrance.

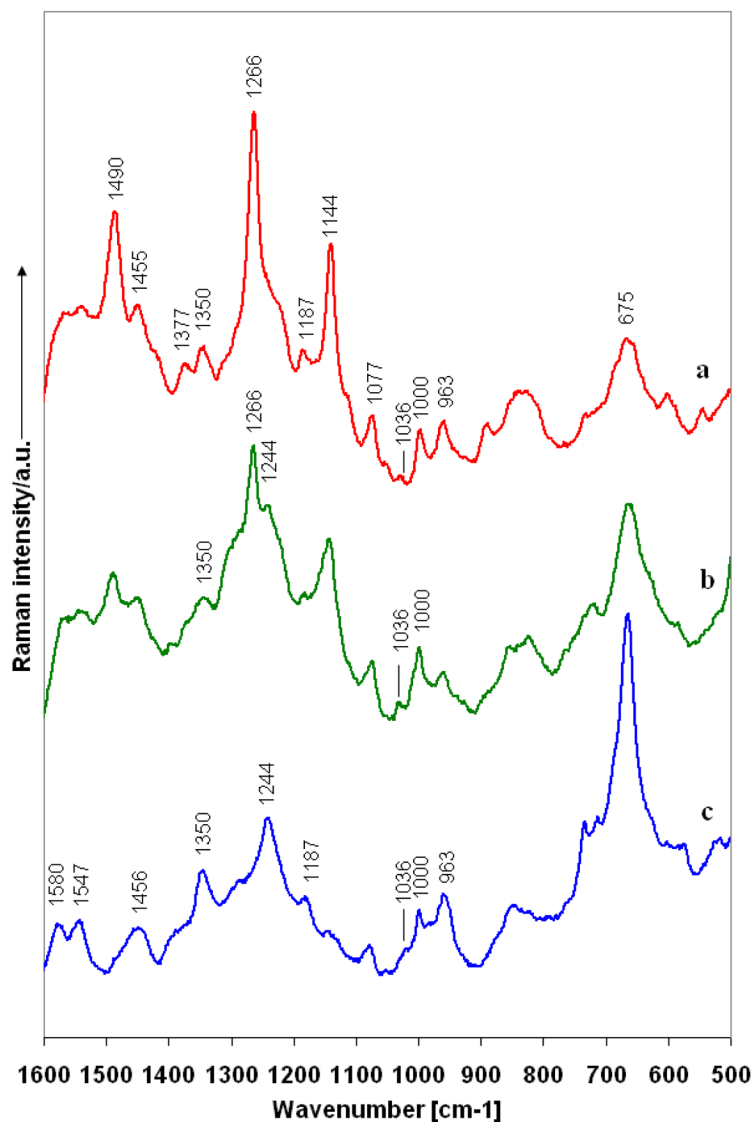


**Figure 3.** SERS spectra of A $\beta$  at (a) 11.5pM (b) 1.15nM (c) 11.5nM after 24 hours in the nanofluidic device. A $\beta$  samples at three different concentrations were prepared in the monomer form and loaded into the nanofluidic device immediately. Seven consecutive scans were taken from the nanoparticle clusters at the entrance to the nanochannel using 50x (NA=0.75) air objective with an 785 nm excitation laser.

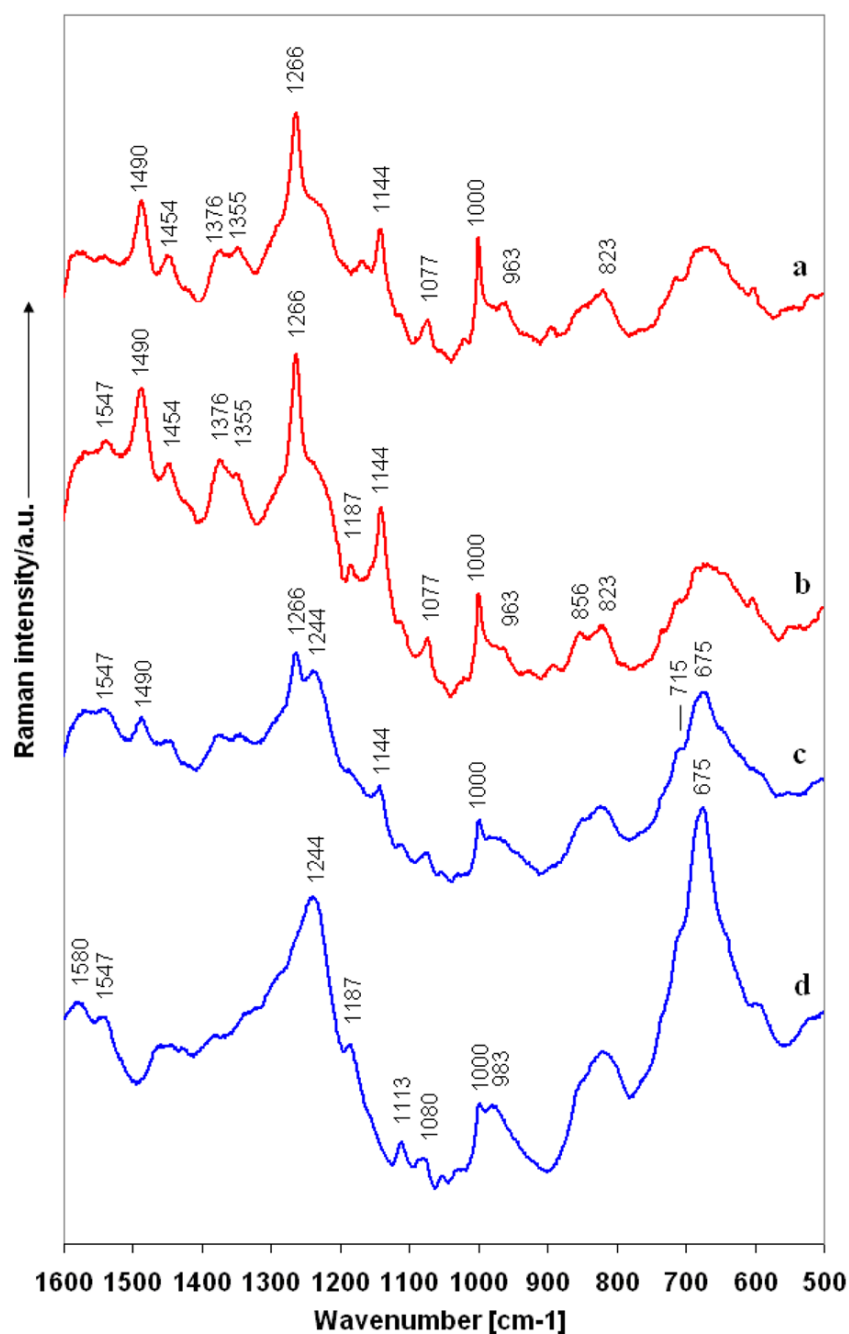


**Figure 4.** SERS spectra of soluble A $\beta$  (6 °C) after (a) 38 hours and (b) 48 hours in the nanofluidic device. Insoluble A $\beta$  oligomer (room temperature) after (c) 38 hours and (d) 48 hours. Both samples were 1.15 nM and had a pH of 6.8 throughout the experiment.



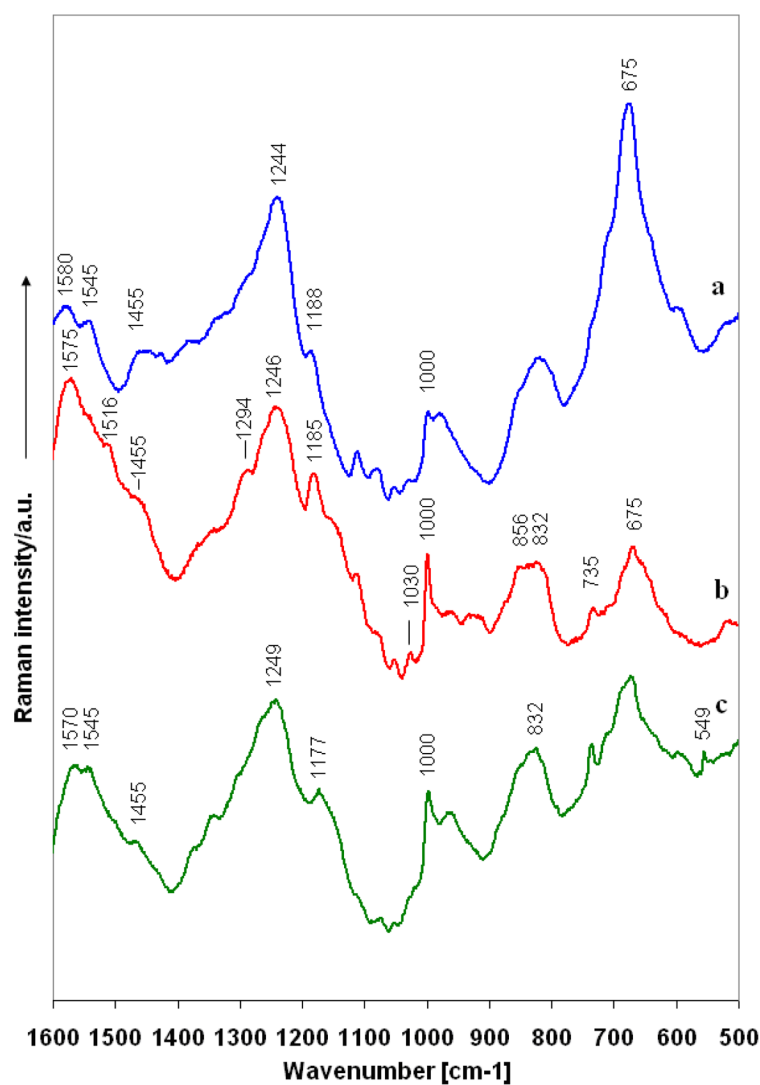


**Figure 5.** SERS spectra of (a) A $\beta$  oligomer (b) albumin and (c) insulin after 48 hours in the nanofluidic device. The three proteins were mixed with gold colloid at 0.1% v/v, to a final protein concentration of 1.15 nM, and loaded into the channel immediately.

**Table I**Assignment of bands in SERS spectra of A $\beta$ 

Wavenumber [cm <sup>-1</sup> ]	Assignment	Reference
675	Tyr	34, 37
823	Tyr doublet	34, 37
856		34, 37
963	n(C-C)	34, 35, 37
1000	Phe (n12)	34–37, 42
1036	Phe (n18 <sub>a</sub> )	34–37
1077	n(C <sub>a</sub> -N)	35, 36
1144	n(CCN)	35, 36
1187	Phe and Tyr	34, 36, 37
1244	Amide III (b-sheet)	35, 42, 43
1266	Amide III (a-helix)	34–36
1350	n(=C-N)	35, 38
1455	d(CH2)	34–38, 42
1490	His	35, 36
1547	Phe, amide II	35, 36
1580	Tyr, n(COO-) and/or Phe	35, 36

n = stretching

d = deformation